

## Energy and Power of Supercapacitor Using Carbon Electrode Deposited with Nanoparticles Nickel Oxide

Nur Hamizah Basri, Mohamad Deraman\*, Mohd Suleman, Najah Syahirah Mohd Nor, Besek Nurdiana Mohamad Dolah, Muhammad Izhar Sahri, Siti Aisyah Shamsudin

School of Applied Physics, Faculty of Science and Technology, National University of Malaysia, 43600 Bangi, Selangor, Malaysia

\*E-mail: [madra@ukm.edu.my](mailto:madra@ukm.edu.my)/[mderaman113@gmail.com](mailto:mderaman113@gmail.com)

Received: 22 September 2015 / Accepted: 9 November 2015 / Published: 1 December 2015

---

Highly porous activated carbon monoliths (ACMs) supercapacitor electrodes (specific surface area  $\sim 1660 \text{ m}^2\text{g}^{-1}$ ) were prepared from KOH-treated pre-carbonized biomass fibers by carbonization ( $\text{N}_2$ ) and activation ( $\text{CO}_2$ ) methods. Nickel oxide nanoparticles were deposited on the surface of the ACMs electrodes for different durations (15, 30, 45, 60 min). The electrodes were characterized by field emission scanning electron microscopy (FESEM), energy dispersive X-ray analysis (EDX), X-ray diffraction (XRD) and  $\text{N}_2$  adsorption-desorption isotherm techniques. Results from electrochemical impedance spectroscopy (EIS), cyclic voltammetry (CV) and galvanostatic charge discharge (GCD) techniques demonstrate that the optimum dipping time range from 15 to 45 min can increase the specific capacitance ( $C_{\text{sp}}$ ) by 30-33 % ( $138\text{-}141 \text{ F g}^{-1}$ ) with respect to the bare electrode. Correspondingly, the composite electrode with deposition time of 15 min offers the maximum improvement of 39 % in maximum specific energy ( $4.30 \text{ Wh kg}^{-1}$ ), but maintaining higher maximum specific power ( $183 \text{ W kg}^{-1}$ ).

---

**Keywords:** Activated carbon monolith, nickel oxide nanoparticles, supercapacitors, electrochemical characteristics, electrochemical impedance spectroscopy, cyclic voltammetry, galvanostatic charge-discharge.

### 1. INTRODUCTION

Supercapacitors or ultracapacitors are energy storage devices that have been well known to have higher power range and better cycling lifespan compared to batteries. Therefore, they have been widely employed in portable electronics, hybrid vehicles and backup energy systems [1]. The performance of supercapacitors is determined by their components namely the electrodes, electrolytes/separators, current collectors, etc. The nature and the properties of the electrode materials

determine the energy storage mechanism in supercapacitors. Depending on the types of electrode materials and charge storage mechanisms, the supercapacitors can be classified as electric double layer capacitors (EDLCs) which employ electrodes from various forms of carbon including activated carbons, carbon nanotubes, graphene etc. [2,3], and redox capacitors or pseudocapacitors which employ transition metal oxides (ruthenium oxide, manganese oxide, nickel oxide etc.) [4–7] or conducting polymer electrodes (polypyrrole, etc.) [8–11].

In EDLCs the energy storage mechanism is associated with the electrostatic accumulation of charges at the electrode-electrolyte interface contributed by electronic charges from electrode and ionic charges from the electrolyte to form electric double layer [12], whereas in redox capacitors the energy is stored and released via fast and reversible redox reactions (referred as faradaic processes) occurring at the surface of electro-active materials [13].

Hybrid configuration of the supercapacitor cells from the two classes can also be fabricated. If the cell comprise of carbon materials as one electrode and metal oxide or conducting polymer as the other electrode the configuration is referred as asymmetric hybrid; and composite hybrid if the cell utilises composite electrodes (carbon-based materials composited with metal oxides or conducting polymers) [6].

The performance of supercapacitors can be enhanced by improving the nature/properties of the current collectors [14], electrolytes [15–17], separators [18–20] and/or electrodes [18,21–24]. For porous carbon electrodes, their improved performance has been made by adding ruthenium oxide [4], nickel oxide [7,25] and manganese oxide [5] into activated carbon to form composite electrodes. Here, the oxide additives were expected to generate faradaic capacitance and/or other effects needed to enhance the supercapacitor performance parameters. Compared to ruthenium oxide, nickel oxide is known to be cheaper and environmental friendly materials for supercapacitor electrodes [26].

In this report, we present a new approach to modify the (ACMs) electrodes wherein the nickel oxide nanoparticles were deposited (for different durations of time) on one side of the (ACMs) electrode that was in contact with separator [21]. The effect of using the nickel coated ACMs electrodes on the supercapacitive performance has been investigated and compared with respect to the bare electrodes. The porous carbon electrodes were prepared from the fibres of oil palm empty fruit bunches (OPEFB) based on our previous method [24]. Porous activated carbon electrodes with high specific surface area (SSA) produced from biomass are widely used in supercapacitors because of their cheap cost, high stability and conductivity [22,23,27,28].

The porosity, structure and microstructure of the electrodes produced in the present study were characterized using  $N_2$  adsorption-desorption isotherm, X-ray diffraction (XRD) and field emission scanning electron microscopy (FESEM) techniques, respectively. The electrochemical characterization of the fabricated supercapacitor cells was carried out using the most common techniques in electrochemical study namely the electrochemical impedance spectroscopy (EIS), cyclic voltammetry (CV) and galvanostatic charge discharge (GCD).

It must be noted here that the EIS data and FESEM/EDX (energy dispersive X-ray analysis) results have also been analysed and partially discussed previously by our group [29] but in the present report we have extended the discussion/interpretation to include the analysis covering the XRD,  $N_2$  adsorption-desorption, CV and GCD data.

## 2. EXPERIMENTAL

### 2.1 Preparation of Electrodes and Supercapacitor cells

Fibres of oil palm empty fruit bunches (OPEFB), a by-product available in large quantities at palm oil mills [30–32], obtained from Sabutek Sdn. Bhd. was first pre-carbonized (Furnace CTMSB46) followed by ball-milling (ball mill AC Motor BS 500-110) and sieving (Matest 24030 Brembate Sopra (BG)) to obtain self-adhesive carbon grains (SACG) with particle size less than 106  $\mu\text{m}$  [28]. The SACG was then mixed with an activation agent (KOH) with the weight ratio of 95 % SACG and 5 % KOH. Mixture of SACG and KOH were added into 300 mL of distilled water and magnetically stirred for 1 h followed by drying in an oven for 24 h at 90 °C [28]. The dried mixture was then milled (model VT Q185) to obtain the finer powder. The green monoliths (GMs) were prepared by pressing 0.75 g of chemically treated powder in 20 mm diameter mould at 250 kg  $\text{cm}^{-2}$  pressure using a press pelletizing machine (VISITEC 2009-Malaysia).

GMs were carbonized up to 800°C (1073 K) in  $\text{N}_2$  gas flow (1.5 L  $\text{min}^{-1}$ ) to produce carbon monoliths (CMs) [30,33–35]. The produced CMs were then physically activated to produce the activated carbon monoliths (ACMs). This was done by increasing the temperature up to 800°C (1073 K) from room temperature with a heating rate of 5 °C  $\text{min}^{-1}$  in a  $\text{CO}_2$  gas flow (1.0 L  $\text{min}^{-1}$ ) for 3 h [27,36,37]. The ACMs produced were polished to obtain 0.4 mm thick and (0.052 to 0.055) g in weight, and extensively washed with distilled water until pH 7 was reached and followed by drying in an oven for 24 h at 90 °C.

The polished ACMs were weighed prior to a deposition process. Four different solutions were prepared for deposition process [7]; (i) 0.1 mol of aqua greenish solution  $\text{Ni}(\text{NO}_3)_2 \cdot 6\text{H}_2\text{O}$  (Sigma Aldrich), (ii) 0.2 mol of clear colour NaOH (R&M Chemicals), (iii) 0.5 mol and, (iv) 1.0 mol of triethanolamine (TEA) (Merck). TEA was used because it can act as a capping agent.

Using a titration method, 0.5 mol of TEA was allowed to flow slowly from the pipette into the magnetically stirring 0.1 mol solution of  $\text{Ni}(\text{NO}_3)_2 \cdot 6\text{H}_2\text{O}$  contained in a beaker. Color of  $\text{Ni}(\text{NO}_3)_2 \cdot 6\text{H}_2\text{O}$  solution was found to get slightly changed to green. The same step was used to mix the 1.0 mol of TEA into 0.2 mol of NaOH. These two mixtures were left for stirring for 10 min. Thereafter, 5 mL of each solution was mixed with each other in the same beaker and placed in oven at 60°C for 60 min. After duration of 60 min, it was observed that the colour of the solution became cloudy which indicates that the deposition process started to begin after ~ 60 min. The deposition was carried out at four different immersion durations; 15, 30, 45 and 60 min, which were respectively labelled as A15, A30, A45 and A60. All of the modified ACMs were annealed at a temperature of 300°C (573 K) for 2 h in the environment of oxygen ( $\text{O}_2$ ) gas to convert the deposited  $\text{Ni}(\text{OH})_2$  to nickel oxide (NiO) [21,29].

The modified ACMs were used as electrodes in symmetrical supercapacitor cells using 316L stainless steel (0.02 mm thick) as current collector, 6 M KOH as electrolyte and a 25  $\mu\text{m}$  thickness of microporous membrane (Celgard, LLC) as a separator.

## 2.2 Physical Characterizations of Electrodes

The porosity characteristics of the ACMs, namely the surface area ( $S_{\text{BET}}$ ), mesopore surface area ( $S_{\text{meso}}$ ), micropore surface area ( $S_{\text{micro}}$ ), volume of mesopore ( $V_{\text{meso}}$ ), volume of micropores ( $V_{\text{micro}}$ ) and average pore diameter ( $D$ ) of ACMs were determined from the adsorption-desorption isotherm data ( $\text{N}_2$  gas at 77 K). The isotherm experimental data were recorded using an accelerated surface area and porosimeter system (ASAP 2010 micromeritic).

The structure of modified ACMs was characterized using an X-ray diffractometer (Bruker AXS Germany D8 Advance) employing  $K_{\alpha}$  Cu radiation of 1.5406 Å. The diffraction pattern of the ACMs was recorded over an angular range  $2\theta$  from  $0^{\circ}$  to  $70^{\circ}$ .

To study the elemental composition and surface morphology of the modified ACMs, the electrodes were characterized using the EDX analysis integrated with FESEM (SUPRA PV 55 model).

## 2.3 Electrochemical Characterizations of Supercapacitor cells

An electrochemical instrument (Solartron SI 1286 and Solartron 1255HF Frequency Response Analyzer) equipped with a Z-view software was used for the electrochemical characterization of the fabricated cells, which was conducted using the EIS, CV and GCD methods. The EIS data were recorded at 10 mV over a frequency range of 100 kHz to 10 mHz. CV measurement was conducted within a potential range of 0 to 1 V, and over a range of scan rate from 1 to 100  $\text{mV s}^{-1}$ . GCD measurement was conducted over a potential range of 0 to 1 V, and at a current density of 10  $\text{mA cm}^{-2}$ .

## 3. RESULTS AND DISCUSSION

### 3.1 Physical Characteristics of Electrodes

**Table 1.** Mass ( $m$ ), dimension (diameter,  $d$  and thickness,  $t$ ) and density ( $\rho$ ) of the green monolith (GM) and activated carbon monolith (ACM) of the bare electrode.

Parameters	GM	ACM
$m$ (g)	0.7381	0.2359
$d$ (mm)	2.3097	1.5317
$t$ (mm)	20.22	14.13
$\rho$ ( $\text{g cm}^{-3}$ )	0.9957	0.9784

Table 1 shows the measured weight ( $m$ ), thickness ( $t$ ) and diameter ( $d$ ) of the GMs and ACMs. These results show 68 %, 34 % and 30 % decrease in  $m$ ,  $t$  and  $d$  of the samples, respectively, after activation [29]. A small change in the density values of the samples occurs after activation. The

carbonization and activation mechanisms explaining these changes are well explained in the literature elsewhere [30].

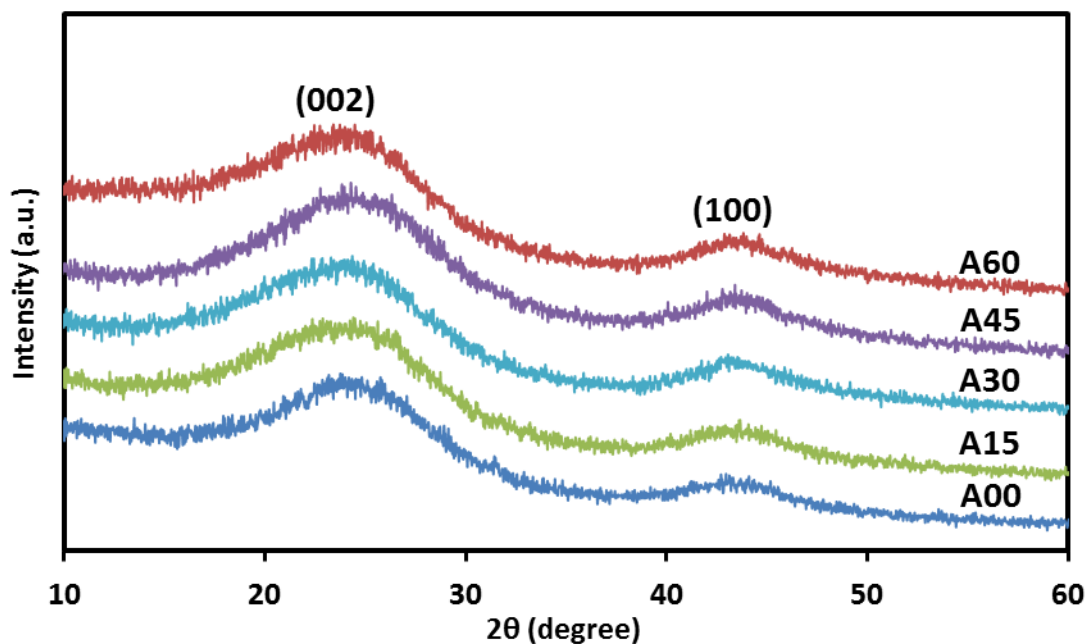


**Figure 1.** X-ray diffractograms for all electrodes.

X-ray diffractograms for all the nickel oxide deposited electrodes (Figure 1) show a similar diffraction pattern without any crystalline peaks contributed by nanoparticles nickel oxide. It was observed elsewhere that a very small nickel oxide aggregation inserted into more than 80 wt% carbon matrix could not be detected by this technique although the high resolution X-ray were applied [38]. Two common broad peaks for carbon materials appear at diffraction angles ( $2\theta$ ) approximately at  $24^\circ$  and  $44^\circ$ , due to reflections from the (002) and (100) planes, respectively as reported elsewhere [37]. These broad signals showed that, after deposition, all the bare electrodes have turbostratic structure with the variation in interlayer spacing ( $d_{002}$ ) only within 3 – 6 % and  $d_{100}$  within 20.5 to 20.6 nm.

**Table 2.** Porosity and microcrystallite parameters for the bare electrode [29].

SAMPLE	ACM
$S_{\text{BET}}$ ( $\text{m}^2 \text{g}^{-1}$ )	1656
$S_{\text{meso}}$ ( $\text{m}^2 \text{g}^{-1}$ )	1011
$S_{\text{micro}}$ ( $\text{m}^2 \text{g}^{-1}$ )	645
$V_{\text{meso}}$ ( $\text{cm}^3 \text{g}^{-1}$ )	0.3002
$V_{\text{micro}}$ ( $\text{cm}^3 \text{g}^{-1}$ )	0.3645
D (nm)	2.20
$d_{002}$ (nm)	3.68
$d_{100}$ (nm)	2.06
$L_c$ (nm)	11.21
$L_a$ (nm)	96.32

Microcrystallites dimensions of the bare electrodes, that is, stack height ( $L_c$ ) and stack width ( $L_a$ ) values calculated from the (002) and (100) diffraction peaks were found to be approximately identical to each other (Table 2); indicating that all of the bare electrodes used for nickel oxide deposition had almost the same structural property.

The adsorption-desorption isotherm data for the bare electrode shown in Figure 2 exhibits a combination of type I and type IV isotherm patterns [39].

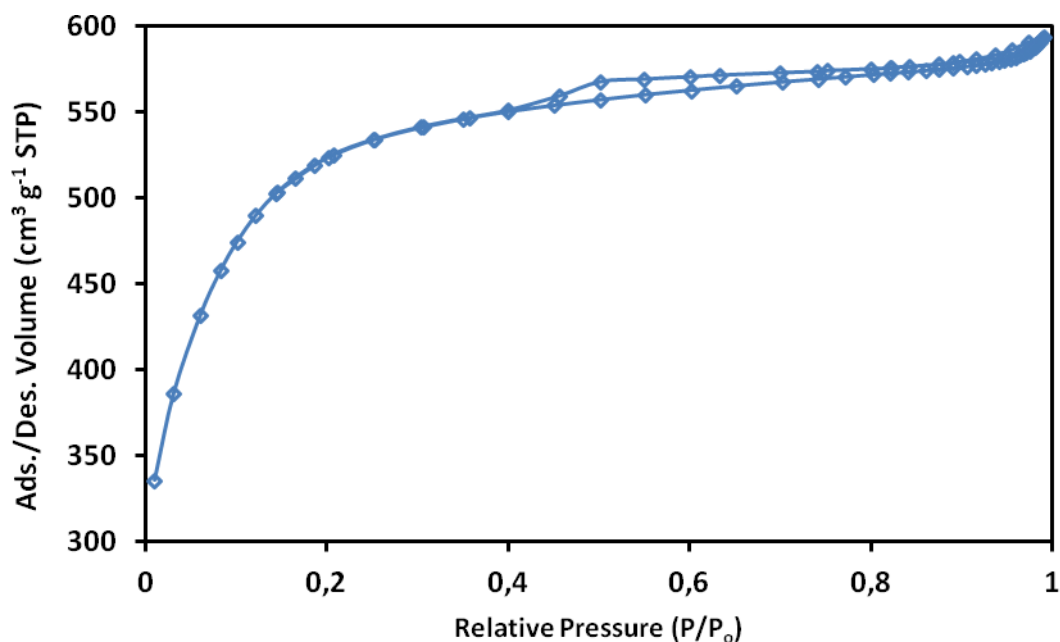


**Figure 2.** Nitrogen adsorption-desorption isotherm for the bare electrode.

This isotherm data indicates that the porous sample has a wide pore size distribution and represents the combination of both mesoporous and microporous pore structures, and resembles to the isotherms for activated carbon from rubber wood sawdust and seaweed carbons [15,27] with large percentage of mesopores (61 %). The average pore diameter lies in the mesopore size range (2 – 50 nm) and is similar to the pore diameter as observed for KOH treated activated carbons reported in the literature [24]. The pore size distribution plots (not shown here) data shows that pores with size larger than the ionic diameter are largely available to accommodate the ions to form double layer at the electrode-electrolyte interface.

The elemental composition and surface morphology of the modified ACMs electrodes characterized using the EDX analysis and FESEM techniques, respectively, were recorded for different regions of the electrodes to study the average bulk properties of the electrode materials. Figure 3 (a), (b) and (c), present the the EDX curves, the table depicting the percentage elemental composition, and the FESEM images for A00, A15 and A60 compositions, respectively.

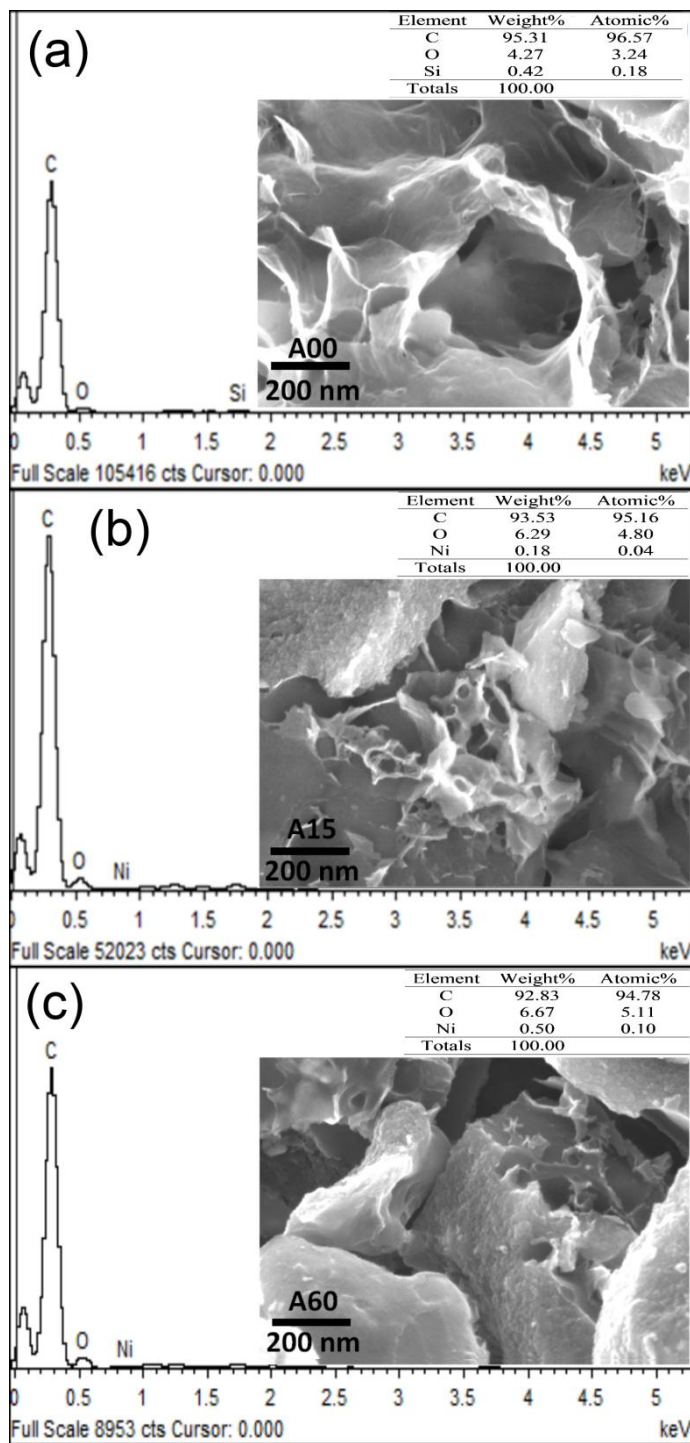


**Figure 3.** FESEM micrographs and EDX spectrums for the (a) bare electrode (A00) [29] and the modified electrode with (b) 15 min (A15)\* and (c) 60 min (A60) [29] deposition time. \*present study

The EDX patterns (Figure 3 (b and c)) show that the intensity of the peaks corresponding to nickel (Ni) and oxygen (O) are vanishingly small which implies a very small proportions of the Ni and O element are present in the electrode compositions A15 and A60 as shown in the table as inset. Contrary to this, no peak in the EDX pattern for the element Ni is observed for the bare electrode A00

and which is an indicative of the absence of the Ni content as shown in the inset table (Figure 3a). Further, it can be observed from FESEM micrographs for the electrode compositions A15 and A60 that as the deposition time increases (that implies increment in the nickel oxide contents) the porosity decreases because some pores are filled by the nickel oxide nanoparticles. The contents of nickel oxide nano particles was confirmed to be about 19 % as opposed to 0 % in the bare electrode.

### 3.2 Electrochemical Characteristics

#### 3.2.1 Electrochemical impedance spectroscopy

EIS analysis gives the fundamental understanding of the electrode/electrolyte interface behaviour, ion diffusion, bulk properties of the electrolytes, etc. The EIS data were analyzed to study the charge-transfer resistance and low frequency capacitance values in different recorded frequency regions and their effects on the performance of the supercapacitor cells.

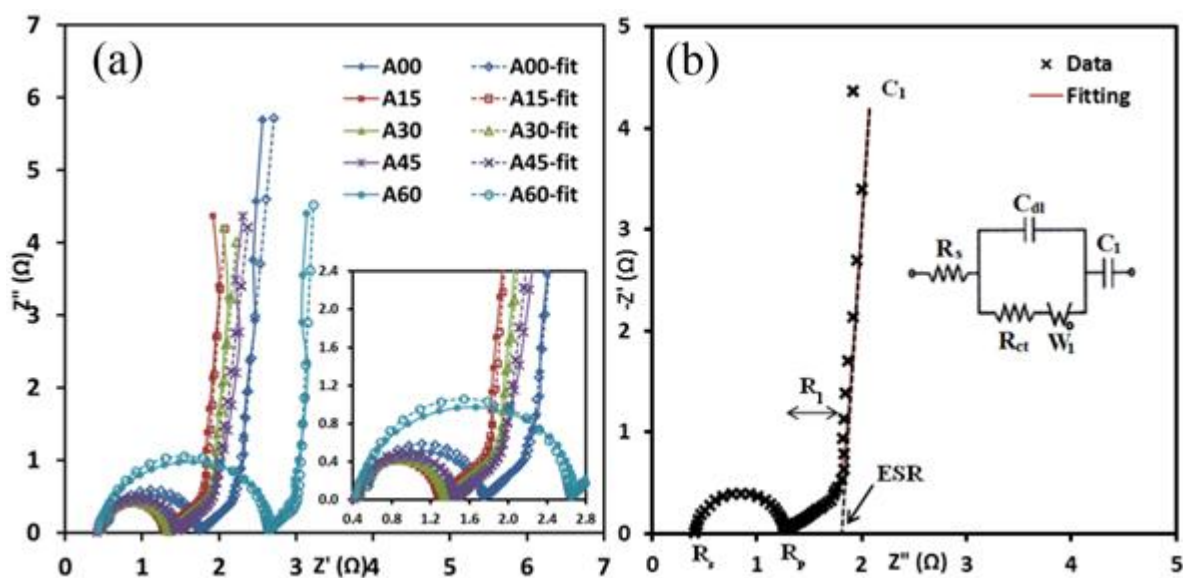


**Figure 4.** (a) Nyquist plots and the overlapped fitted impedance curves for all cells and (b) Fitted impedance curve (1 MHz to 0.01 Hz) obtained by simulating the equivalent circuit of A15 cell [29].

Figure 4 (a) shows the impedance spectra (Nyquist plots) of all the cells under investigation. This represents a semicircle in the high frequency region, Warburg line in the intermediate frequency region and almost a vertical line in the low frequency region. The Figure 4 (a) (inset) shows the Warburg diffusion region showing a slope at around 45° from the horizontal axis; the steeper the slope the higher the diffusion capability of ions entering the pores. The steep rising trend of the imaginary part  $Z''$  with respect to its real part  $Z'$  of the impedance as the frequency varies from low to high value reflects the capacitive behaviour of the cells. The specific capacitance was evaluated at 10 mHz using

the relation:  $C = -(2\pi f_0 Z'')^{-1}$ . By dividing this value with the average mass of electrode, the value of limit capacitance or specific capacitance ( $C_{sp}$ ) in the circuit was obtained.

The Nyquist plots in Figure 4 (a) were further analysed by a simulation method using the modified Randal's equivalent circuit [2,40] that comprises of  $R_s$  (contact resistance),  $C_{dl}$  (double layer capacitance),  $R_{ct}$  (charge-transfer resistance),  $W$  (Warburg component) and  $C_1$  (specific capacitance), as shown in Figure 4 (b). The fit can perform with errors less than 5 %. The  $R_s$  represents the resistance of the electrolyte-electrode-current collector. The double layer capacitance ( $C_{dl}$ ), which is in parallel connection with  $R_{ct}$ , represents the double layer capacitance (generally lying in the scale of  $\mu F$ ) between the ionic charge of the electrolytes and the electronic charges of the electrodes.

The fitting of the data in Figure 4 (a) was carried out using the Z-view software based on this modified Randle circuit. The obtained values of fitting parameters,  $R_s$ ,  $R_{ct}$ ,  $W$ ,  $C_{dl}$  and  $C_1$  are shown in Table 3. The  $R_s$  values in the Table 3 are small and typically satisfactory for the cells with activated carbon electrodes and KOH electrolyte [2,41]. A moderate change in the values of  $R_{ct}$  for 00 to 45 min. deposition time is observed in, but a significant change occurs when deposition time is well above 45 min., implying that the excessive deposition time will adversely affect the electrode performance (Table 3). The similar behaviour can be observed for the ESR values which are obtained from the intercept of extrapolated capacitive line with the real axis.

**Table 3.** Parameters values from fitted impedance equivalent circuit [29](Permitted by TTP Publisher).

Parameters	Supercapacitor cells				
	A00	A15	A30	A45	A60
$R_s$ ( $\Omega$ )	$0.54 \pm 1.3\%$	$0.43 \pm 1.0\%$	$0.46 \pm 0.9\%$	$0.46 \pm 1.1\%$	$0.49 \pm 1.5\%$
$R_{ct}$ ( $\Omega$ )	$1.17 \pm 0.8\%$	$0.84 \pm 0.7\%$	$0.87 \pm 0.6\%$	$0.97 \pm 0.7\%$	$2.11 \pm 0.7\%$
$W_R$ ( $\Omega$ )	1.50	1.61	1.72	1.51	1.23
$W_T$	3.95	6.06	6.71	5.46	4.29
$W_P$	0.4716	0.4785	0.4740	0.4651	0.4853
$Z''$ ( $\Omega$ )	5.69	4.36	4.20	4.36	4.40
$C_{sp}$ ( $F g^{-1}$ )	108	138	142	135	132
$f_k$ (m Hz)	24.7	22.7	20.2	19.8	14.9
$\tau_o$ (s)	40.55	44.07	49.50	50.50	67.20
ESR ( $\Omega$ )*	2.20	1.79	1.85	1.92	3.02

\*estimated by extrapolating graph technique via Origin Pro 8.0

The connection of  $W$  in series with the  $R_{ct}$  is associated with the position of Warburg region which is located between the semicircle and the spike in Nyquist plot. As shown in Figure 4 (a) (inset) the Warburg impedance region/line was observed for all the cells. The length of this line represents the three different components namely diffusion resistance ( $W_R$ ), diffusion coefficient ( $W_T$ ) and Warburg exponent ( $W_P$ ), expressed as  $A(j\omega)^{-n}$  [42].

Coefficient  $A$  explains the properties of the electrode surface and the ionic species of the electrodes and depends on the values of  $W_R$  and  $W_T$ ; where  $W_T$  is calculated using equation  $l^2/D$  (s),  $l$ , being length of diffusion layer and  $D$  the binary electron-ion diffusion coefficient [43]. Meanwhile  $j$  ( $=\sqrt{-1}$ ) is the imaginary number,  $\omega$  is the angular frequency and  $n$  is the Warburg exponent equal to  $W_P$ . Value of  $n$  varies from 0 to 1, the minimum value represents a resistance, and the max value ( $n = 1$ ) indicates a pure capacitive behaviour. The values of  $W_P$  obtained from the fitting for all cells (that are close to 0.5, as listed in Table 3), indicate the Warburg transition line has a slope of almost  $45^\circ$  and this corresponds to the porous nature of the electrodes [42,44].

It can be observed from the considerable difference in the values of  $W_R$  and  $W_T$  (Table 3) that the behaviour of ions diffusion into pores over the Warburg frequency region is notably sensitive to the effect of variation in deposition time; however a small difference in the values of  $W_P$  is observed for all the cells which implies that the deposition process has insufficient effect to change the bulk properties i.e. the bulk porosity of bare electrode [43,45].

The EIS data in Figure 4 can also be analysed using Bode plot (the plot in which real part ( $Z'$ ) and imaginary part ( $Z''$ ) of impedance ( $Z$ ) are plotted against frequency, Figure 5), from which one can calculate the values of characteristic response time,  $\tau_o$ , a parameter that determines the rate capability of the supercapacitors [46]. The lower value of  $\tau_o$  is always preferred because it corresponds to higher power delivery of the supercapacitor cells. It is reciprocally related to the resonant (response) frequency  $f_o$ , at which the real and imaginary parts of impedance,  $Z$  (i.e.  $Z'$  and  $Z''$ ) as a function of frequency intersect each other or in other words it is the frequency at which the resistive and capacitive contributions to the total impedance,  $Z$  are equal [47,48]. It can be observed from Table 3 that an increase in the duration of deposition time results in increased value of  $\tau_o$ , that may be probably due to the blockage of some pores by the deposited particles. These values of  $\tau_o$  are comparable to those as reported elsewhere [36].

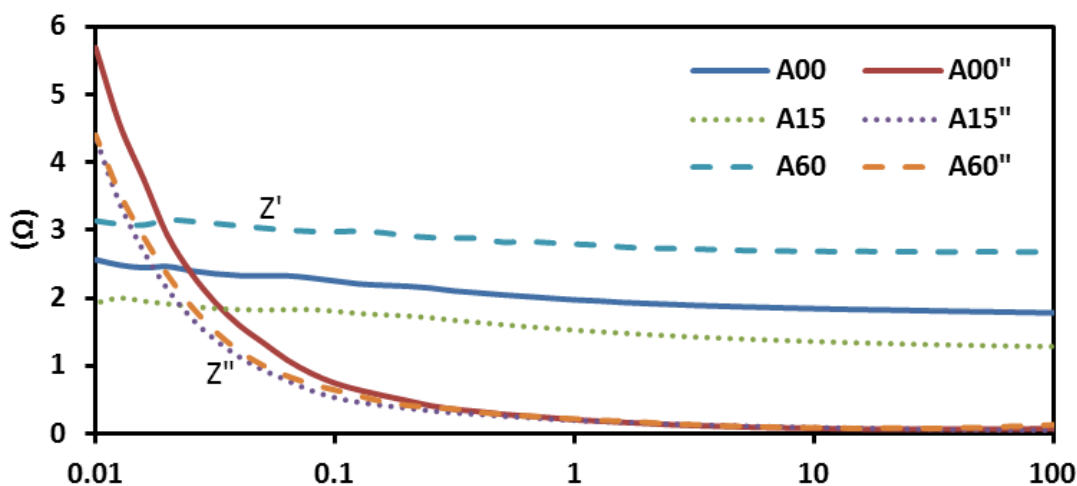
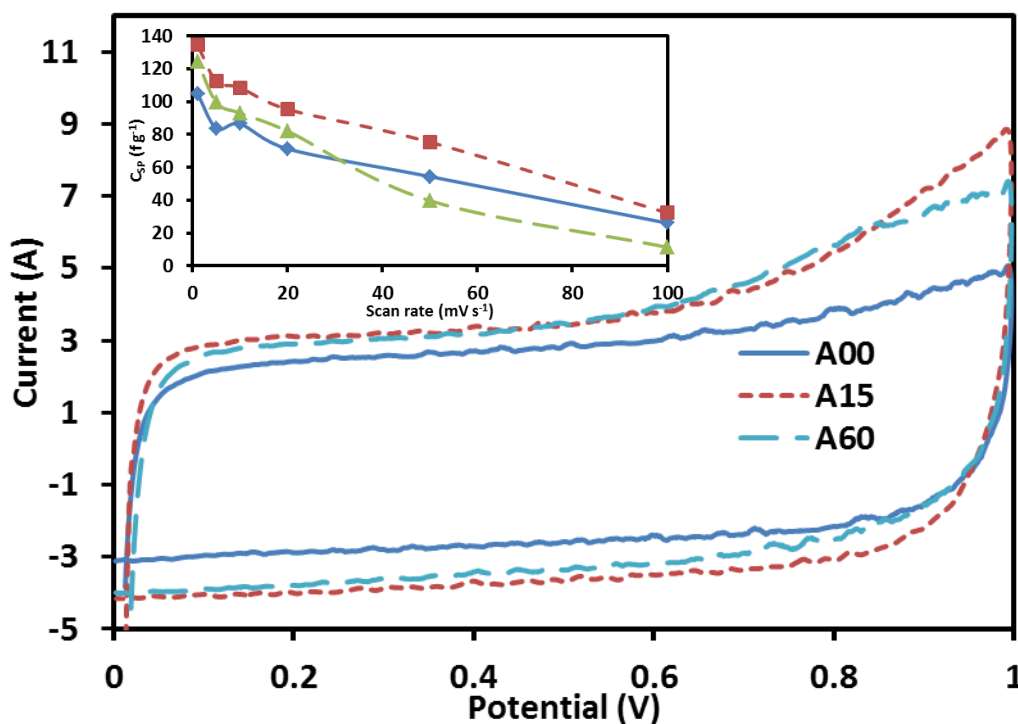


Figure 5. Bode Plots for different cells.

### 3.2.2 Cyclic voltammetry

Figure 6 shows the comparative CV profiles of all the supercapacitor cells recorded at room temperature at a scan rate of  $1 \text{ mV s}^{-1}$ . The CV curves show almost rectangular shape which is generally observed for carbon based supercapacitors. These features of the CV indicate the capacitive behavior of the cells. Curves for A30 and A45 electrodes based cells are not shown in the Figure 6 because the results are close to each other and lie in the middle range of other results with insignificant difference. It is noticeable that compared to the A00 electrodes based cell, the CV curves for the A15 to A60 cells show sharper increase in the voltammetric current as voltage approaches  $\sim 1 \text{ V}$ , a feature possibly arising from the nickel oxide deposition.

Further, the voltammograms for A00, A15 and A60 cells show the absence of redox peaks, which demonstrates that the amount of NiO deposited was insufficient to provide pseudo-capacitive effect to the electric double layer capacitance.



**Figure 6.** Cyclic voltammetry for A00, A15 and A60 cells.

A similar behavior has also been observed for the CNTs/carbon cloth electrodes doped with NiO additive reported in the literature [25,49,50]. In these cases, it can be assumed that the modified electrodes have inadequate amount of deposited nickel oxide and that the role of NiO here is possibly purely on the aspect of altering the surface properties of the electrodes, such as surface functionality, wettability and/or morphology, rather than contributing pseudo-capacitive effect.

**Table 4.** Specific capacitance ( $C_{sp}$ ), specific power (P) and specific energy (E) for all cells. \* present study

Cell	$C_{sp}$ (EIS, 10m Hz) [29]	$C_{sp}$ (CV, $1 \text{ mV s}^{-1}$ )*	$C_{sp}$ (GCD, $10 \text{ mA cm}^{-2}$ )*	ESR ( $\Omega$ )*	P ( $\text{W kg}^{-1}$ )*	E ( $\text{Wh kg}^{-1}$ )*
A00	108	105	106	1.99	183	3.09
A15	138	134	143	1.80	183	4.30
A30	142	137	145	1.88	182	4.19
A45	135	135	122	2.01	178	4.18
A60	132	125	130	2.24	173	3.66

Table 4 presents the values of  $C_{sp}$  calculated at a scan rate of  $1 \text{ mV s}^{-1}$  using the equation  $C_{sp} = 2i/(sm)$ , where  $i$  is the current,  $s$  is the scan rate, and  $m$  is the average mass of the electrodes. These values appear to be in good agreement with that determined by other methods. Figure 6 (inset) shows the variation of specific capacitance  $C_{sp}$  with the scan rate increasing from  $1 \text{ mV s}^{-1}$  to  $100 \text{ mV s}^{-1}$ . It can be noticed that the  $C_{sp}$  for the A15 cell is higher than the other cells over the entire range of the scan rate as shown in Figure 6 (inset). Further, it can be observed that as the scan rate increases up to a value of  $100 \text{ mV s}^{-1}$ , the  $C_{sp}$  value decreases by  $\sim 75 \%$  with respect to the initial value and this can be due to the fact that the ions find insufficient time to penetrate through the pores and hence giving rise to inefficient double layer formation [20].

### 3.2.3 Galvanostatic charge discharge

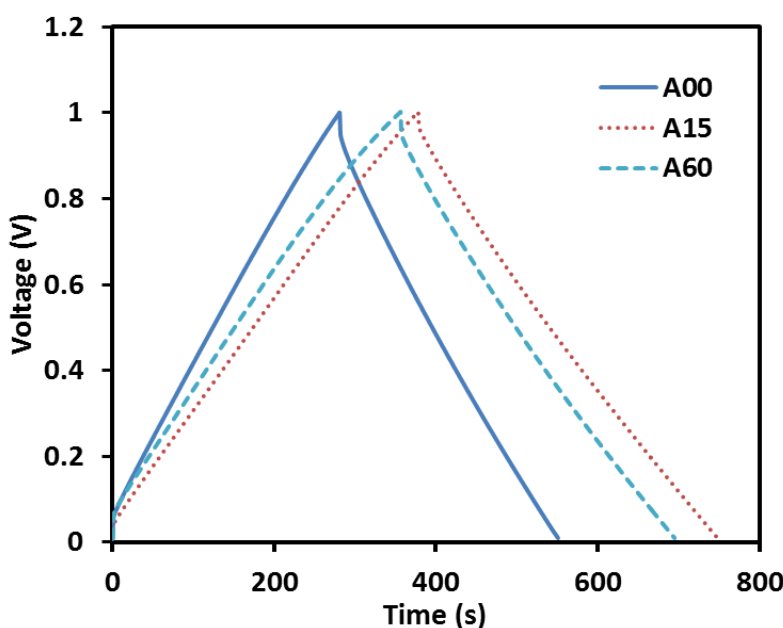
**Figure 7.** Galvanostatic charge discharge for A00, A15 and A60 cells.

Figure 7 shows the comparative GCD curves for the cells fabricated with the electrodes A00, A15 and A60 cells. It can be noticed that all the curves have similar isosceles triangular shape which represents a typical pattern of satisfactory capacitive behavior for carbon-electrode based cells. However, it can be observed that the area under the curve or charge and discharge period corresponding to each electrode is different, being maximum for the A15 electrode based cell which demonstrates that A15 cell exhibits superior capacitive performance as compared to the other cells. This behaviour is consistent with that observed in CV and EIS studies.

Table 4 shows the values of  $C_{sp}$  calculated from the GCD curves using an equation  $C_{sp} = -2i\Delta t/(m\Delta V)$ , where  $\Delta V$  is the voltage difference,  $\Delta t$  is the discharge period,  $i$  is the current density and  $m$  is the average mass of the electrodes. It can be seen that the results follow the same trend as exhibited by the CV and EIS studies. Results showing the similar trend have also been reported in the literature [14,36].

Additional feature that can be seen in Figure 7 is a slight voltage drop at the beginning of discharge curve; this voltage drop corresponds to the equivalent series resistance (ESR) of the supercapacitor cell, associated with the diffusion limited mobility of the electrolyte ions transporting through the pores of the electrodes [23]. The ESR values calculated using the relationship  $V_{drop}/2i$ , where  $V$  is voltage and  $i$  is current density, range from 1.80  $\Omega$  (A15) to 2.24  $\Omega$  (A60) which are relatively small for all cells but consistent in their trend with those estimated from EIS analysis.

These values are also comparable with those reported for the carbon based electrodes derived from biomass and its processed bi-product waste such as oil palm empty fruit bunches composites with CNTs [22], gamma radiated oil palm empty fruit bunches [23], rubber wood sawdust [14] and rubber scrap tires [51] which exhibit the ESR values of 0.26 to 1.46  $\Omega$ , 0.102 to 0.507  $\Omega$ , 0.018 to 0.34  $\Omega$  and 0.34 to 0.40  $\Omega$ , respectively.

### 3.2.4 Ragone Plots

The specific power,  $P$  and specific energy,  $E$  of the supercapacitor cells calculated from the GCD curve data using equation  $P = Vi/m$  and  $E = Vit/m$  respectively, where,  $V$  is voltage (excluding the  $V_{drop}$  occurring at the beginning of the discharge curve)  $t$  is time (in hour), can be plotted against each other and generally referred as Ragone plots. The calculated values of  $E$  and  $P$  were analyzed and plotted (Figure 8) and it was found that all the cells exhibit almost an ideal knee shaped pattern for E-P relationship.

However, of all the compositions, the A15 electrode based cell has the superior E-P relationship, with the highest maximum  $E$  (4.30 W h kg<sup>-1</sup>) and  $P$  (183 W kg<sup>-1</sup>) values as shown in Table 4. This result indicates that an optimum duration of depositing NiO on electrodes surface is able to produce a well improved E-P relationship for the supercapacitors. It should be noted here that a lot of reported literature on the E-P relationship have been published for carbon based supercapacitors. Recently, Nor et. al [23] have reported a summary of achievement for  $E_{max}$  and  $P_{max}$  values for more than 15 reported results and they found  $E_{max}$  and  $P_{max}$  values ranging from 0.3 x 10<sup>-3</sup> to 10.2 W h kg<sup>-1</sup> and 40 to 3600 W kg<sup>-1</sup> respectively, for aqueous electrolyte supercapacitors.

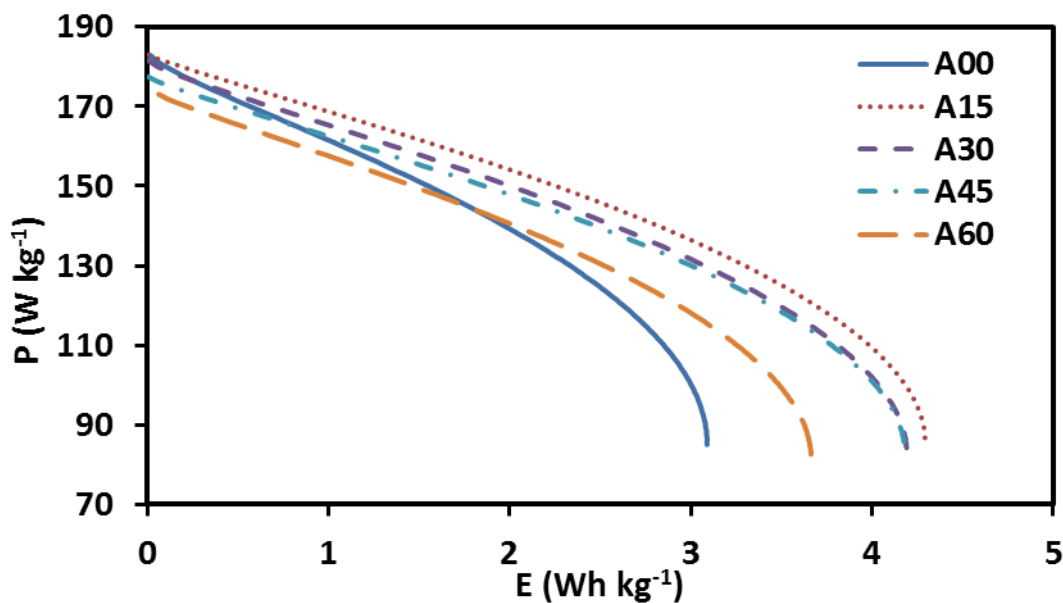


**Figure 8.** Specific power against specific energy, or Ragone plots, for all cells.

#### 4. CONCLUSION

The supercapacitor activated carbon monoliths (ACMs) porous electrodes (specific surface area  $\sim 1660 \text{ m}^2 \text{ g}^{-1}$ ) from KOH-treated pre-carbonized biomass fibers (derived from OEFB) were prepared by carbonization ( $\text{N}_2$ ) and activation ( $\text{CO}_2$ ) methods. Chemical bath deposition technique was used to deposit nickel oxide (NiO) nanoparticles on the surface of the electrodes wherein the ACMs were dipped in  $\text{Ni}(\text{NO}_3)_2$  and NaOH solutions for a duration ranging from 0 to 60 min and followed by annealing at  $300^\circ\text{C}$  for 2 h. These electrodes were used to fabricate the supercapacitor cells and it was observed that for the composite electrodes and over a range of dipping time interval (from 15 to 45 min), the specific capacitance value was found to increase by (30-33 %) that corresponds to the value of (138-141)  $\text{F g}^{-1}$  and the equivalent series resistance to decrease by (8 – 19 %) that corresponds to the value of (2.02-1.79)  $\Omega$  with respect to the bare electrode with corresponding specific capacitance and equivalent series resistance values of  $\sim 106 \text{ F g}^{-1}$  and  $2.20 \Omega$ , respectively. Further, the performance of the supercapacitor cells utilizing the composite electrode with deposition duration of 15 min has recorded the maximum improvement of 39 % in specific energy ( $4.30 \text{ Wh kg}^{-1}$ ) along with no reduction in specific power as compared to the bare (non-NiO coated) electrodes ( $3.09 \text{ Wh kg}^{-1}$ ).

#### ACKNOWLEDGEMENTS

The authors are grateful to the research grants from MOE (ERGS/1/2012/STG05/UKM/01/2), (FRGS/2/2013/ST05/UKM/01/1), UKM (UKM-DIP-2014-027, UKM-Industri-2013-026), MOSTI (03-01-02-SF1118) and the support of CRIM of UKM with instruments. The authors also thank to Mr. Saini Sain for help with the laboratory work and for the kind collaborative work of Department of Physics and Astrophysics, University of Delhi, India.

## References

1. Y. Ren, H. Wei, X. Huang, B. Yang, J. Wang, J. Ding, *Int. J. Electrochem. Sci.*, 9 (2014) 7206.
2. G. Xu, C. Zheng, Q. Zhang, J. Huang, M. Zhao, J. Nie, X. Wang, F. Wei, *Nano Res.*, 4 (2011) 870.
3. C. Zheng, X. Zhou, H. Cao, G. Wang, Z. Liu, *J. Power Sources*, 258 (2014) 290.
4. J.M. Sieben, E. Morallón, D. Cazorla-Amorós, *Energy*, 58 (2013) 519.
5. T. Huang, Z. Qiu, D. Wu, Z. Hu, *Int. J. Electrochem. Sci.*, 10 (2015) 6312.
6. S.-G. Hwang, S.-H. Ryu, S.-R. Yun, J.M. Ko, K.M. Kim, K.-S. Ryu, *Mater. Chem. Phys.*, 130 (2011) 507.
7. K. Lota, A. Sierczynska, G. Lota, *Int. J. Electrochem.*, 2011 (2011) 1.
8. R.B. Rakhi, W. Chen, H.N. Alshareef, *J. Mater. Chem.*, 22 (2012) 5177.
9. N. Li, Y. Xiao, C. Xu, H. Li, X. Yang, *Int. J. Electrochem. Sci.*, 8 (2013) 1181.
10. C. Hu, S. He, S. Jiang, S. Chen, H. Hou, *RSC Adv.*, 5 (2015) 14441.
11. Y. Shi, L. Pan, B. Liu, Y. Wang, Y. Cui, Z. Bao, G. Yu, *J. Mater. Chem. A*, 2 (2014) 6086.
12. A. Elmouwahidi, Z. Zapata-Benabithé, F. Carrasco-Marín, C. Moreno-Castilla, *Bioresour. Technol.*, 111 (2012) 185.
13. U.M. Patil, R.R. Salunkhe, K.V. Gurav, C.D. Lokhande, *Appl. Surf. Sci.*, 255 (2008) 2603.
14. E. Taer, M. Deraman, I.A. Talib, S.A. Hashmi, A.A. Umar, *Electrochim. Acta*, 56 (2011) 10217.
15. M.P. Bichat, E. Raymundo-Piñero, F. Béguin, *Carbon*, 48 (2010) 4351.
16. X. Zhang, X. Wang, L. Jiang, H. Wu, C. Wu, J. Su, *J. Power Sources*, 216 (2012) 290.
17. X. Du, W. Zhao, Y. Wang, C. Wang, M. Chen, T. Qi, C. Hua, M. Ma, *Bioresour. Technol.*, 149 (2013) 31.
18. I. Stepniak, A. Ciszewski, *J. Power Sources*, 195 (2010) 5130.
19. H. Yu, Q. Tang, J. Wu, Y. Lin, L. Fan, M. Huang, J. Lin, Y. Li, F. Yu, *J. Power Sources*, 206 (2012) 463.
20. N.S.M. Nor, M. Deraman, R. Omar, E. Taer, R. Farma, N.H. Basri, B.N.M. Dolah, *AIP Conf. Proc.*, 1586 (2014) 68.
21. B. Wen, S. Zhang, H. Fang, W. Liu, Z. Du, *Mater. Chem. Phys.*, 131 (2011) 8.
22. B.N.M. Dolah, M. Deraman, M.A.R. Othman, R. Farma, E. Taer, N.H. Basri, I.A. Talib, R. Omar, N.S.M. Nor, *Mater. Res. Bull.*, 60 (2014) 10.
23. N.S.M. Nor, M. Deraman, R. Omar, R. Farma, N.H. Basri, B.N.M. Dolah, N.F. Mamat, B. Yatim, M. Norizam, *Energy*, 79 (2015) 183.
24. N.H. Basri, M. Deraman, S. Kanwal, I.A. Talib, J.G. Manjunatha, A.A. Aziz, R. Farma, *Biomass Bioenergy*, 59 (2013) 370.
25. W. Bohua, Z. Shichao, F. Hua, *Rare Met.*, 30 (2011) 661.
26. G. Huang, S. Xu, Y. Cheng, W. Zhang, J. Li, *Int. J. Electrochem. Sci.*, 10 (2015) 2594.
27. E. Taer, M. Deraman, I.A. Talib, A. Awitdrus, S.A. Hashmi, A.A. Umar, *Int. J. Electrochem. Sci.*, 6 (2011) 3301.
28. R. Farma, M. Deraman, A. Awitdrus, I.A. Talib, E. Taer, N.H. Basri, J.G. Manjunatha, M.M. Ishak, B.N.M. Dollah, S.A. Hashmi, *Bioresour. Technol.*, 132C (2013) 254.
29. N.H. Basri, M. Deraman, R. Daik, M.T.M. Ayob, M.I. Sahri, N.S.M. Nor, B.N.M. Dolah, S. Soltaninejad, *Adv. Mater. Res.*, 1112 (2015) 236.
30. M. Deraman, R. Omar, A.G. Harun, *J. Mater. Sci. Lett.*, 17 (1998) 2059.
31. M. Deraman, *J. Phys. D Appl. Phys.*, 27 (1994) 1060.
32. M. Deraman, M.P. Ismail, M.M.D. Said, *J. Mater. Sci. Lett.*, 14 (1995) 781.
33. M. Deraman, R. Omar, S. Zakaria, I.R. Mustapa, M. Talib, N. Alias, *J. Mater. Sci.*, 7 (2002) 3329.
34. M. Deraman, S. Zakaria, R. Omar, A.A. Aziz, *Jpn. J. Appl. Phys.*, 39 (2000) 1236.
35. A. Awitdrus, M. Deraman, I.A. Talib, R. Farma, R. Omar, M.M. Ishak, N.H. Basri, B.N.M. Dolah, *Adv. Mater. Res.*, 501 (2012) 13.

36. R. Farma, M. Deraman, I.A. Talib, R. Omar, J.G. Manjunatha, M.M. Ishak, *Int. J. Electrochem. Sci.*, 8 (2013) 257.
37. Awitdrus, M. Deraman, I.A. Talib, R. Omar, M.H. Jumali, E. Taer, M.M. Saman, *Sains Malaysiana*, 39 (2010) 83.
38. N. Rinaldi-Montes, P. Gorria, D. Martínez-Blanco, A.B. Fuertes, L. Fernández Barquín, J. Rodríguez Fernández, I. de Pedro, M.L. Fdez-Gubieda, J. Alonso, L. Olivi, G. Aquilanti, J.A. Blanco, *Nanoscale*, 6 (2014) 457.
39. K.S.W. Sing, D.H. Everett, R.A.W. Haul, L. Moscou, R.A. Pierotti, J. Rouquerol, T. Siemieniowska, *Pure Appl. Chem.*, 57 (1985) 603.
40. A. Di Fabio, A. Giorgi, M. Mastragostino, F. Soavi, *J. Electrochem. Soc.*, 148 (2001) A845.
41. S.L. Zhang, Y.H. Song, X.G. Li, W. Li, *Adv. Mater. Res.*, 239-242 (2011) 797.
42. Y. Kumar, G.P. Pandey, S.A. Hashmi, *J. Phys. Chem. C*, 116 (2012) 26118.
43. J. Fernández, J. Molina, A.I. del Río, J. Bonastre, F. Cases, *Int. J. Electrochem. Sci.*, 7 (2012) 10175.
44. A. Laheäär, S. Delpoux-Ouldriane, E. Lust, F. Béguin, *J. Electrochem. Soc.*, 161 (2014) A568.
45. Y. Kumar, G.P. Pandey, S.A. Hashmi, *J. Phys. Chem. C*, 116 (2012) 26118.
46. J.R. Miller, -, in: Proc. Eighth Int. Semin. Double Layer Capacit. Similar Energy Storage Devices, 1998.
47. F. Lufrano, P. Staiti, M. Minutoli, *J. Power Sources*, 124 (2003) 314.
48. C.G. Liu, M. Liu, F. Li, H.M. Cheng, *Appl. Phys. Lett.*, 92 (2008) 67.
49. G.H. Yuan, Z.H. Jiang, A. Aramata, Y.Z. Gao, *Carbon*, 43 (2005) 2913.
50. H.-Y. Chang, H.-C. Chang, K.-Y. Lee, *Vacuum*, 87 (2013) 164.
51. P. Zhao, Y. Han, X. Dong, C. Zhang, S. Liu, *ECS J. Solid State Sci. Technol.*, 4 (2015) 35.